Combined Use of Satellite Observations and the RIM for Assessing Recovery from Natural Disasters

Changyong Cao, Wenhui Wang, Yan Bai, Xi Shao, Sirish Uprety, and Hong-Lie Qiu

Abstract

In this study, we explore using satellite observations to assess community recovery from natural disasters such as fires and hurricanes, supplementing the Resilience Inference Model (RIM). The RIM model has been successfully used to quantify recoveries from hurricanes along the Gulf Coast, but it relies on long-term population changes over years or decades. Our approach integrates satellite observations to enhance recovery assessment with a shorter latency of weeks or months. Using fire, vegetation, and night light data from the Visible Infrared Imaging Radiometer Suite (VIIRS) with daily global observations, Sentinel-2, Landsat-8, and Geostationary Operational Environmental Satellite/ Advanced Baseline Imager, we quantitatively evaluate fire intensity, light outage, and urban greenness changes, along with subsequent recovery, focusing on the 2023 Maui fire and selected hurricane cases along the Gulf Coast. This approach complements the RIM model by introducing quantifiable physical parameters with shorter latency, particularly beneficial in areas where census data are either unavailable or unreliable.

Introduction

Natural disasters such as hurricanes and fires are detrimental to property and life. Extensive studies have been conducted to assess the effect of these disasters, which have occurred more frequently in recent years. Hurricanes have caused the most deaths and destruction among all recorded weather disasters in U.S. history (NOAA 2023). From 2020 to 2022, there have been 60 weather and climate disasters with losses exceeding $1 billion. The total cost of damages from 1980 to the present is more than $2.6 trillion, almost equivalent to the gross domestic product of Italy or France. July and August 2023 were the warmest months on record, and there were more sea surface temperature anomalies than any other month in NOAA's 174-year record. In August 2023, Southern California experienced the first tropical storm in 84 years, Hurricane Hilary, with gusty winds and torrential rain that broke all daily rainfall records for the area. At the same time, the Maui wildfires on 8 August 2023, caught everyone by surprise. They destroyed more than 2,000 structures, caused $4 to $6 billion in losses from property damage and business interruption, with the town of Lahaina practically destroyed (Schulz and Collins 2023). More than 100 people died in the Maui fire. It will take years for Lahaina to recover from this disastrous event.

Researchers have studied the social–ecological resilience, vulnerability, hazards, and risk assessment to natural disasters such as hurricanes and fires and recognized the importance of quantifying them (Cutter *et al.* 2003; Vogel 2006; Adger and Brown 2010; Tierney and Oliver-Smith 2012). Lam *et al.* (2016) introduced the Resilience Inference Measurement (RIM) model to quantify resilience to climate-related hazards for 52 counties along the northern Gulf of America in the United States. The model uses three elements: exposure, damage, and recovery indicators, to denote two relationships: vulnerability and adaptability, and the model employs both K-means clustering and discriminant analysis to derive the resilience rankings, thus enabling validation and inference.

Although the RIM model has been demonstrated in studying the resilience of the community to natural disasters along the Gulf Coast, we also recognized that the model primarily relies on social and economic data such as population change as well as other census statistics, which typically have long latency for quantifying the resilience after natural disasters. The period of the resilience study using this model can range from years to decades. In the current study, we explore expanding the use of the RIM model to other environmental factors that can be readily derived from remotely sensed satellite data that have shorter latency for natural disaster assessments. This extension of the RIM model to the short-term recovery with satellite observation assessments complements Lam's RIM model. In particular, we demonstrate the use of NOAA Visible Infrared Imaging Radiometer Suite (VIIRS) observations and other high resolution data for quantifying the short- and long-term recovery from major disasters in days, months, and years. The VIIRS observed night light intensity by the day/night band and the urban greenness index from the imagery bands derived from daily observations were used for assessing the recovery of Lahaina in the Maui wildfire, as well as the recovery from hurricanes along the gulf coast. This paper is structured as follows: after the introduction, we review the RIM model, followed by a review of the various satellite instrument capabilities in observing disaster events and recovery. In the third section, we present the methodology for developing the indicators of recovery from VIIRS and other satellite observations, and the results are presented in the following section, with further discussion related to the RIM model. The final section provides a summary and conclusion.

Review of the RIM Model

As pointed out by Lam *et al.* (2016), the U.S. National Research Council report defined resilience as "the ability to prepare and plan for, absorb, recover from, and more successfully adapt to adverse events" (National Research Council 2012). At the same time, the Intergovernmental Panel on Climate Change (2007) considered vulnerability a function of three factors: exposure, sensitivity, and adaptive capacity. The RIM model (Lam *et al.* 2016) adopted the definition by the National Research Council report and considers resilience as

Changyong Cao is with National Oceanic and Atmospheric Administration (NOAA), National Environmental Satellite, Data, and Information Service (NESDIS), Center for Satellite Applications and Research (STAR).

Wenhui Wang, Yan Bai, Xi Shao, Sirish Uprety, and Hong-Lie Qiu are with Cooperative Institute for Satellite Earth System Studies (CISESS), Earth System Science Interdisciplinary Center (ESSIC), University of Maryland, College Park.

Corresponding author: Changyong Cao (Changyong.Cao@noaa.gov)

Received January 29, 2024, accepted November 28, 2024.

Photogrammetric Engineering & Remote Sensing
Vol. 51, No. 7, July 2025, pp. 407–417.
0099-1112/22/407–417

doi: 10.14358/PERS.24-00050R2

comprising both aspects of vulnerability and adaptability. The conceptual RIM model is best summarized in Lam *et al.* (2016) (Figure 1).

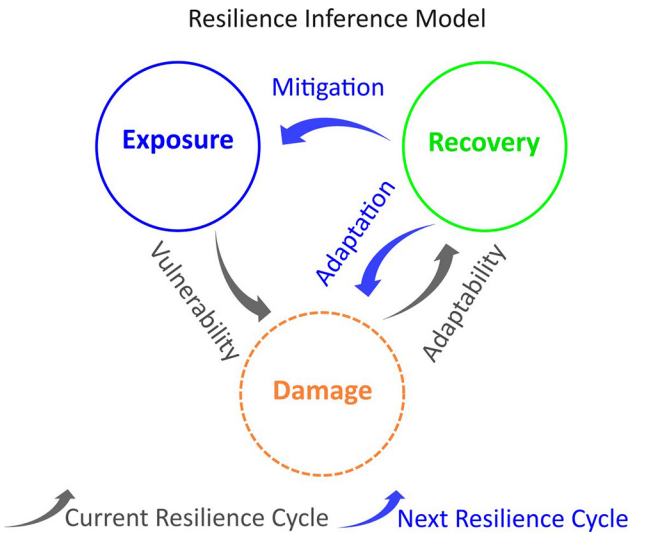

Figure 1. Lam's RIM model (modified from Lam *et al.* 2016).

For a given community, such as Lahaina (for wildfire) or New Orleans (for hurricanes), its exposure to hazards leads to vulnerability, which will have a high probability of causing damage in an unexpected event such as a hurricane or fire. The community may recover and hopefully recover faster next time due to adaptability and developing mitigation to be prepared for the next cycle in which the community will become more resilient (Cutter *et al.* 2003; Walker *et al.* 2006a; Lam *et al.* 2016; Bathiany *et al.* 2024).

Although conceptually the RIM model is relatively easy to understand, quantifying resilience is challenging (Walker *et al.* 2006b; Peduzzi *et al.* 2009; Lam *et al.* 2016, 2018; Bathiany *et al.* 2024). To address this issue, resilience is considered a broader concept that includes aspects of both vulnerability and adaptive capacity over time in the RIM model, and therefore, the model considers three elements: exposure, damage, and recovery, and two relationships: vulnerability and adaptability. A time interval of 10 years was used in the RIM model to compute the exposure and damage to coastal hazards. Statistical data including census from 1998 to 2008 were used as a key variable in the RIM model for the study area of Gulf Coast counties, which included five states: Texas, Louisiana, Mississippi, Alabama, and Florida. The three elements for each county were defined as: (1) the exposure to hazards, represented by the number of times hurricanes or climate-related hazards hit a community; (2) the damage from exposure to hazards, represented by the property damage; and (3) the recovery, represented by population growth (Lam *et al.* 2016).

However, Lam *et al.* (2016) acknowledged that using population change alone may not be sufficient to indicate recovery. They suggested that other indicators could include economic, environmental, infrastructural, and social factors, such as development intensity. Nevertheless, no specific details were provided because some of these variables could be difficult to define and obtain data for. Also, aggregated statistical data are known to have a long latency from time of the event to the time when the data becomes available publicly, which is a drawback of using population as the major indicator of long-term recovery.

In the current study, we explore using remotely sensed data from several satellites to quantify the recovery after natural disasters. In particular, satellite observation time series from the night light intensity observed from NOAA's VIIRS day/night band (DNB), and the urban greenness index calculated from the Normalized Difference Vegetation Index (NDVI) in both short-term and long term are used as indicators of recovery, hopefully to complement the RIM model, which heavily relies on population growth as recovery indicator. Furthermore, disaster events such as the Maui fire are analyzed using multiple satellite data including Geostationary Operational Environmental Satellite (GOES) Advanced Baseline Imager (ABI), VIIRS, Landsat, *Sentinel-2*, and hyperspectral data from Earth surface Mineral dust source InvesTigation (EMIT), at different spatial, temporal, and radiometric resolutions to quantify the damages from the disasters.

Methodology and Satellite Observation Data

In this section, we first examine the various satellites available for detecting the Maui Lahaina fire and their advantages and limitations. Then we focus on using VIIRS fire bands and the DNB to study the fire. The analysis is also extended to hurricane cases later.

Satellite Capabilities and Limitations for Observing Disaster Events: The Lahaina Fire Case

Since the first satellite launch of Explorer 1 by the United States in 1958, the number of Earth observation satellites has skyrocketed especially in recent years, with the proliferation of small satellite launches. The global space industry revenue is more than $300 billion a year. The number of orbital space launches worldwide reached 174 in 2022, the highest number since the beginning of the Space Race in 1957 (Statista 2023). Not all of them are for Earth observations. According to the eoPortal satellite missions catalogue maintained by the European Space Agency (eoPortal 2023), there are more than 1000 Earth observation satellites in space today.

However, not all satellites can observe disasters like fire and hurricanes. There are four major constraints for each satellite sensor: spatial, spectral, radiometric, and temporal resolution and associated performance characteristics. Although it is known that hurricanes cause more damage in coastal regions such as along the coast of the Gulf of America and wildfires occur more frequently in arid to semi-arid climate regions, the precise time and location of such events are not well predicted. Very often, a satellite instrument can be perfectly designed for disaster monitoring, such as those in the Committee on Earth Observation Satellites Disaster Monitoring Constellations, the satellites unfortunately may not be in the right place at the exact time of such events as discussed below. In addition, each satellite mission has data downlink bandwidth limits, availability, and latency limitations. Here, we use the Maui Lahaina fire to illustrate the capabilities and limitations of various satellite observations.

The Lahaina fire, on the northwest coast of Maui Island, Hawaii, practically destroyed the city of Lahaina, with more than 100 deaths, and more than 200 homes destroyed. It is among the biggest tragedies in the modern history of disaster events. It occurred so quickly from 8 to 9 August 2023, precipitated by drought, the spread of non-native grasslands (Piper *et al.* 2023), downed power lines, and hurricane-force winds from Hurricane Dora, moving across the Pacific despite being more than 500 km away. According to the official results from the investigation by the U.S. Fire Administration, on 8 August 2023, wind-driven wildfires on the island of Maui destroyed more than 2,200 structures and caused about $5.5 billion in damages. The most significantly affected area was the historic district of Lahaina, where more than 100 lives were lost. On April 17, 2024, Hawaii attorney general released the Lahaina Fire Comprehensive Timeline Report (Kerber and Alkonis 2024) on the devastating August 2023 fire that led to the fatalities, widespread destruction, and devastating community effects.

Which satellite captured the Lahaina fire while it was burning? Figure 2 and Table 1 provide a snapshot of selected satellites over Lahaina between the evening of 8 August and early morning of 9 August 2023, when the fire was burning. Our orbital analysis shows that three satellites captured this horrific event: GOES-18 West (positioned at 137.2 W longitude, 0 latitude) observed the Lahaina fire every 10 minutes (Mode 6) with 2-km resolution in the 3.9-μm and other thermal infrared bands. It shows that the maximum fire radiative power was observed on the evening of 8 August local time between 6 and 9 PM; meanwhile, *Landsat-8* captured the Lahaina fire once at 10:25 PM local time on 8 August with its 1.6 μm and thermal infrared thermal infrared sensor (TIRS) bands at 30- and 100-m resolution, respectively. On the other hand, VIIRS from three satellites (Suomi National

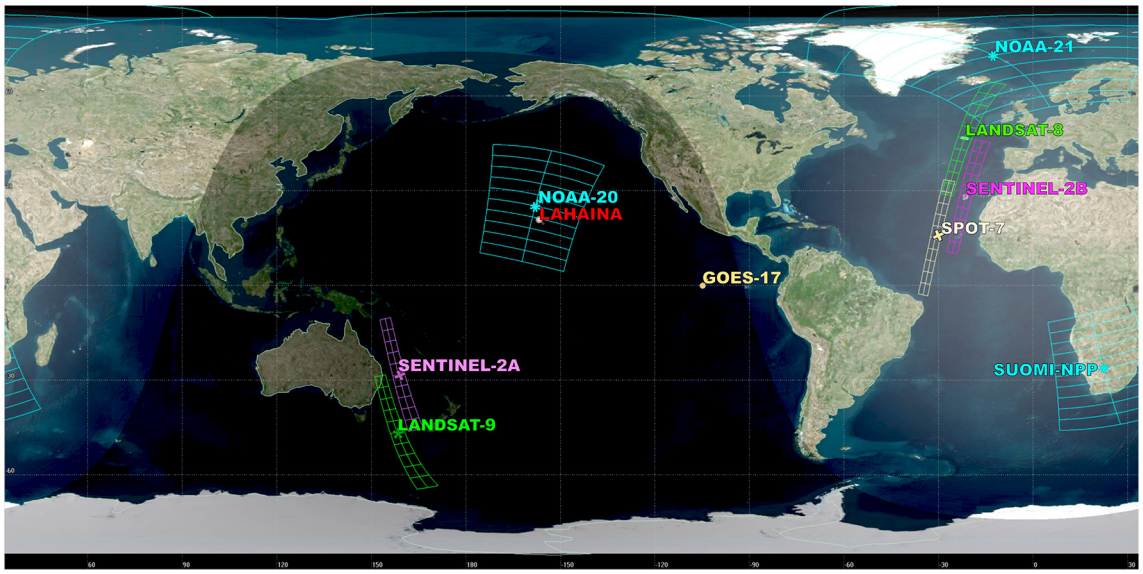

Figure 2. Location of multiple satellites on 9 August 2023, 2:14 A.M. local time (local time was UTC −10 hours) during the Lahaina fire.

Table 1. Satellite overpass for the Maui site during the fire (4 PM on 8 August to 2 PM on 9 August)

Satellite/Sensor	Observed the Lahaina Fire (Local Overpass Time)	Temporal Resolution/ Revisit Time	Spatial Resolution	Spectral Channel	Comments
GOES West/ABI	All times	10-minute (mode 6 full disk)	2000 m	3.9 μm, IR	Video available (but no Mesoscan); 14 bits for the 3.9-μm channel
Landsat-8/9	8 August 10:25 PM	Every 8 to 16 days	30 m	1.6 μm, thermal infrared sensor	L8 overpass but saturated; L9 observed after fire. (14 bits)
S-NPP/VIIRS	9 August 1:25 AM 9 August 2:17 PM	Twice daily (~1:30 AM/PM)	375 m	I4 and M13 (4 μm), SWIR, DNB, IR	12 bits; 14 bits (DNB night)
NOAA-20/VIIRS	9 August 2:14 AM 9 August 1:26 PM	Twice daily (~1:30 AM/PM)	375 m	I4 and M13 (4 μm), SWIR, DNB, IR	12 bits; 14 bits (DNB night)
NOAA-21/VIIRS	9 August 2:37 AM 9 August 1:48 PM	Twice daily (~1:30 AM/PM)	375 m	I4 and M13 (4 μm), SWIR, DNB, IR	12 bits; 14 bits (DNB night)
Sentinel-2A/2B	No overpass during fire	Every 5–10 days	20 m	SWIR and RGB	Overpass before and after the fire (on 13 August), 12 bits
SPOT7	No overpass during fire		6 m		Overpass after the fire (data not used for this study), 12 bits
JPL EMIT	18 August 2023	On demand	60 m	Hyperspectral 380–2500 nm	16 bits; spectral resolution 7.4 nm

Note: All observation data (L1b) by instruments listed in Table 1 were used in this study, with the exception of SPOT7. ABI = Advanced Baseline Imager; DNB = Day/Night Band; JPL = Jet Propulsion Laboratory; EMIT = Earth surface Mineral dust source InvesTigation; GOES = Geostationary Operational Environmental Satellite; IR = infrared; S-NPP = Suomi National Polar-Orbiting Partnership; SWIR = Short-Wave InfraRed; VIIRS = Visible Infrared Imaging Radiometer Suite.

Polar-Orbiting Partnership [S-NPP], *NOAA-20*, and *NOAA-21*) with 375-m spatial resolution (as well as other thermal bands with 750-m spatial resolution) observed the Lahaina fire multiple times. *Sentinel-2*, with a high spatial resolution of up to 10 m, captured the fire in the central part of Maui around noon local time on 8 August and then after the fire event on 13 August but unfortunately did not capture the Lahaina fire, which started spreading in the afternoon of 8 August. Similarly, the EMIT instrument on the International Space Station (ISS) acquired hyperspectral data from 0.4 to 2.5 μm with ~7.4-nm spectral resolution and 60-m spatial resolution (Green *et al.* 2020; Green 2022; Thompson *et al.* 2024) over the Lahaina area on 18 August 2023 (after the fire), and the data were also used for analysis in this study. The multi-satellite observations over the same location during a disaster event can complement each other and help better capture the spatial and temporal evolution of the fire and assess its spread and damage.

The Lahaina fire provides an example of the advantages and shortcomings of various satellites. Although GOES West has high temporal resolution with 10-minute mode 6 full-disk observations (up to 30 seconds if Mesoscan were activated to scan two overlapped regions), it has a low spatial resolution of 2 km, and therefore no details of the fire at the city level can be observed. ABI covers the entire city in just a few pixels. On the other hand, *Sentinel-2* has a high spatial resolution of 10 m, but it was not there to observe the fire because it has a temporal coverage every 5 to 10 days. In contrast, the VIIRS instrument has a moderate resolution and observed the fire twice daily from each of the three satellites. It is quite possible that other satellite sensors may have captured the fire but mostly coincidentally during the time window of this event. In addition, the revisit time of 5 to 10 days is further affected by clouds, which appear frequently on the island of Maui. Other active sensors, such as the synthetic aperture radar on *Sentinel-1*, can penetrate the cloud, but can only detect surface roughness instead of fire.

Analysis of Data from Multiple Satellite Observations

Given the various limitations of different sensors on several satellites, we focus on using VIIRS observations to study the Maui Lahaina fire

event and the subsequent damage and recovery of the Lahaina city. From the ABI observations of GOES West, we found that the maximum intensity of the Lahaina fire occurred around 7:30 PM on 8 August 2023 local time. GOES West ABI could have captured the fire with Mesoscale mode if this was requested and prescheduled, which would be able to monitor the event with 30-second time intervals. However, no other satellite observed the fire during this time window of maximum intensity (Table 1).

Landsat-8 had a near nadir overpass over Lahaina on 8 August at 10:25 PM local time (Figure 3). Analysis of the radiometric values of the Landsat TIRS bands show that these bands are saturated over a large area so the hottest pixel (T_{max}) cannot be identified. According to *Landsat-8* TIRS specification, the saturation temperature is at 360 K, which is far below the temperature of the intense fire at many locations in Lahaina (https://landsat.gsfc.nasa.gov/satellites/landsat-8/spacecraft-instruments/thermal-infrared-sensor/tirs-requirements/). Analysis of the *Landsat-8* band 6 at 1.6 µm shows that relatively fewer pixels (about 40 in the north Lahaina area) were saturated. The hottest area with saturated pixels appears in the northern part of Lahaina city. We estimated that the maximum radiometric intensity of the fire occurred at 20.89N, −156.68W (UTM: 741163, 2311962, zone 4), although the maximum values are unknown because it is saturated (flagged as 65535 in the Landsat data).

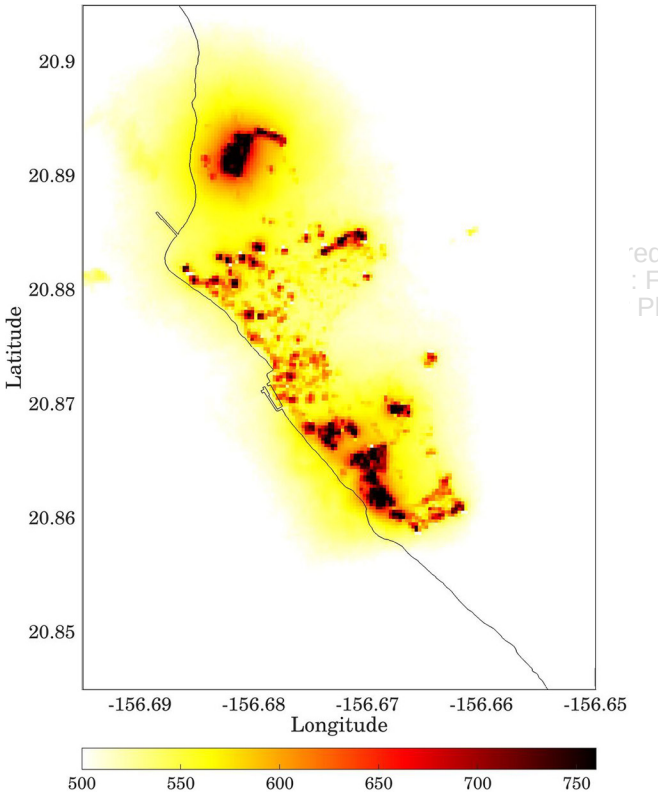

Figure 3. *Landsat-8* OLI (Operational Land Imager) observed the Lahaina Maui fire at 10:25 PM local time on 8 August near nadir with its 1.6-µm channel. The color legend shows brightness temperature in kelvin (black represents saturated pixels).

Following the *Landsat-8* observation, VIIRS observed the fire multiple times at midnight and in the early morning of 9 August 2023. In the following section, we performed more detailed analysis of the location of the highest fire intensity using VIIRS data.

As discussed previously, the launch of S-NPP VIIRS in 2011 marked a new era of operational moderate resolution imaging in the sun-synchronous polar orbiting satellite, succeeding the heritage sensors such as Moderate Resolution Imaging Spectroradiometer (MODIS) and Advanced Very High Resolution Radiometer (AVHRR). The S-NPP VIIRS has performed well over a decade by now (Cao *et al.* 2014, 2021), providing global Earth observations twice daily around 1:30 PM equator crossing local time ascending node (or 1:30 AM descending). The primary channel for fire detection is the 4.05-µm channel known as M13, with a moderate spatial resolution of 750 m at nadir, and a brightness temperature dynamic range up to 634 K with its dual gain design, which has a distinct advantage over many sensors for which saturation is common at such high temperatures for this channel. The M13 channel is complemented by the spectrally similar imaging band of I4, which has a spatial resolution of 375 m at nadir, but a saturation brightness temperature of ~367 K. Two VIIRS active fire products are typically generated independently using the available 750- and 375-m resolution data. The 750-m fire product inherited the MODIS algorithm, adapted to VIIRS channels M5, M7, M11, M13, M15, and M16. The 375-m fire product uses the VIIRS imaging bands of I1–I5, complemented by channel M13, to detect and characterize subpixel active fire (Csiszar *et al.* 2014).

Separately, the Nightfire algorithm (Elvidge *et al.* 2013) detects and characterizes subpixel hot sources using multispectral data collected globally, each night, by using VIIRS visible, near-infrared, short-wave infrared (SWIR), and mid-wave infrared channels. The primary detection band is in the VIIRS SWIR, centered at 1.6 µm for both VIIRS I3 and M10 bands. At night, this band is sensitive to high radiant emissions associated with gas flares, biomass burning, volcanoes, and industrial sites such as steel mills. Planck curve fitting of the hot source radiances produces temperature (K) and emission scaling factor.

On the other hand, the VIIRS Day/Night Band, with its extremely high sensitivity to night lights, can also detect fires at night. It is known that this band can detect ~1000 optical watts of total energy in the 0.4 to 0.9 spectral range within a pixel of 750 × 750 square meters. However, this band is mostly used for night light observations like city lights. In this study, we developed a time series of night lights for Lahaina to study its destruction due to fire and the subsequent recovery.

In this study, we first investigated the evolution of the Lahaina fire hour-by-hour using GOES West observations to identify the time at which the maximum fire intensity was reached. Then, we used the VIIRS imaging band to zoom in on the area at the maximum fire temperature around the time to further identify the location of the maximum fire intensity. Once the time and location of the maximum fire intensity were identified, we extracted the radiometric data for this location to develop a time series using the VIIRS night light intensity and NDVI (as a proxy for urban greenness index) derived from the VIIRS imaging bands I2 and I1 to study the recovery of urban greenness and infrastructure in the process. It is noted that both MODIS and AVHRR have observed the Maui fire because they both have global coverage daily, and the AVHRR on Metop-B and -C satellites are in the mid-morning orbit similar to that of MODIS on Terra, whereas MODIS on Aqua is in a similar orbit as that of the S-NPP, *NOAA-20*, *NOAA-21* satellites. However, the spatial resolutions of both AVHRR and MODIS for the thermal infrared bands are lower than that of VIIRS, and neither one has the night light observation capabilities of VIIRS DNB.

As shown in Figure 2, *NOAA-20* had a near nadir overpass over Lahaina in the early morning of 9 August. Analysis of the band I4 (with 375-m spatial resolution at ~4 µm) shows that only one pixel was saturated due to very high brightness temperature. This pixel was identified by geographic location as 20.8986N, −156.6799W (pixel location: 3810/73 in the granule), which is in the vicinity of the location of the hottest spot (T_{max}) shown in the *Landsat-8* image a few hours earlier. On the other hand, it is also known that when a *NOAA-20* or S-NPP pixel is saturated, it could "roll over" to a lower value, which could make the pixel value an outlier compared to the background (Wang *et al.* 2022). The apparent saturated pixel is identifiable because it shows an unrealistic brightness temperature (208 K) far below the background temperature. It is also possible that other pixels may have rolled over to a temperature closer to the background temperature, which would be difficult to distinguish. This raises the question of whether the saturated pixel is the real hottest pixel (T_{max}) and whether other saturated pixels are nearby.

To address this issue, we further investigated using the VIIRS M13 band, which has a nearly identical spectral response to I4 except it has a lower spatial resolution of 750 m at its nadir and saturates at much higher temperatures. Geometrically, these two bands match well. The 2 × 2 pixels in the I4 band are nested in one M13 pixel. It is also known that because the M13 is a dual gain band, the pixels are aggregated in the cross-track direction at about a 3:1 ratio at the nadir. The unaggregated data are downlinked from the satellite and the aggregation occurs in the ground processing system. An unaggregated M13 band has a higher spatial resolution (an intermediate product), although this is only for the cross-track direction, whereas in the along-track direction, it is still 750 m per pixel. Three unaggregated M13 pixels at the nadir make up for one standard (aggregated) M13 pixel at nadir, and the unaggregated pixel is rectangular in shape (250 × 750 m in size). Nevertheless, the unaggregated data would provide additional information about the I4 band saturated pixel.

Analysis of the same saturated pixel location in I4 is identified as having a brightness temperature of 407.01 K in M13 standard product, and its corresponding unaggregated data from this M13 pixel shows that the brightness temperature values are 439.41, 392.06, and 366.68 K, respectively, before aggregation. According to the Planck function, the aggregation must be performed in the radiance space because the radiance and brightness temperature are highly nonlinear in this spectral region. The radiance values for these three unaggregated pixels are 33.70, 12.69, and 6.78 W/m²-sr-μm, respectively, or an average of 17.72 W/m²-sr-μm, which matched the brightness temperature of 407.01 K of the M13 aggregated pixel and did not saturate the M13 because this channel can measure up to 634 K due to its dual gain design. As a result, this suggests that the saturated pixel in I4 was the "hottest pixel" (T_{max}) at the time, and this location (20.8986N, −156.6799W) is therefore used for subsequent analysis including the time series. Further cross-checking with the fire radiative power (FRP) product (https://firms.modaps.eosdis.nasa.gov/; https://firms.modaps.eosdis.nasa.gov/usfs/map/#d:24hrs;@-156.62,20.89,11.64z) also confirmed this location and shows that the highest FRP is 73.66W retrieved using the FRP algorithm with I4 and I5.

With the hottest (T_{max}) location identified, we also explored the hyperspectral observations of the Maui Lahaina fire to evaluate this hottest spot site. EMIT is a NASA Jet Propulsion Laboratory (JPL) mission to use state-of-the-art imaging spectroscopy across the visible to short wavelength infrared (VSWIR) spectral region to measure the Earth's arid land dust source regions. The EMIT was launched to the ISS on 14 July 2022. EMIT measures the spectral range from 380 to 2500 nm with 285 contiguous spectral channels. Spectral cross-track uniformity and spectral instantaneous field of view uniformity for this VSWIR imaging spectrometer are key requirements for EMIT spectroscopy (Thompson *et al.* 2024).

Ideally, we would want to compare the spectral changes of the Lahaina site using EMIT observations before and after the fire event to study the change. However, although there was a good data set shortly after the fire, there were no EMIT observations of the site before the fire with clear sky. As a result, we used the Airborne Visible/InfRared Imaging Spectrometer (AVIRIS) data (Green *et al.* 1998) to analyze the spectral signature of the site before the fire. Although the only recent AVIRIS data available for Lahaina region is from 2018, it still served well for the purpose of analyzing the region before the fire (it had a similar solar zenith angle to the EMIT observation after the fire). The main reason for using AVIRIS is that only one EMIT data set was available from before the fire, but the Lahaina area was covered by clouds. However, after the fire on 18 August 2023, it was a clear-sky day, and we were able to analyze the spectra with the EMIT data set. We performed this analysis with the assumption that both AVIRIS and EMIT represent typical urban spectra for this geographic area. In addition, both the instruments observe the site at similar solar zenith angles. To reduce the registration error, we have used similar size regions of interest (~300 × 300 m) for EMIT and AVIRIS. The top-of-atmosphere (TOA) reflectance spectra over the hottest region is compared before and after the fire (Figure 4). The spectra for the hottest area (before fire) indicates strong reflectance over visible, near-infrared, and short-wave infrared regions. However, the TOA reflectance dropped sharply for the same location (black curve) after the fire for the spectral region below 1.7 μm. The drop in signal is mainly due to the darkening of the surface at this location and loss in green vegetation after the fire. The drop in the reflectance before and after the fire is as expected and is quantified using the Normalized Burn Ratio (NBR), a measure of the burn severity (https://www.usgs.gov/landsat-missions/landsat-normalized-burn-ratio). The NBR is an index that measures the difference in reflectance between near-infrared and shortwave infrared light to indicate the presence of burned areas. NBR values range from −1 to 1, with higher values indicating healthy vegetation and lower values indicating burned areas. The NBR for the hottest area was 0.43 before burn, and reduced to −0.18 after burn. The sharp decrease in the NBR index for the hottest area indicates the change in the spectral characteristics of the land cover (darkening) after burn. The large difference in NBR before and after fire also indicates the severity of the burn over the hottest location.

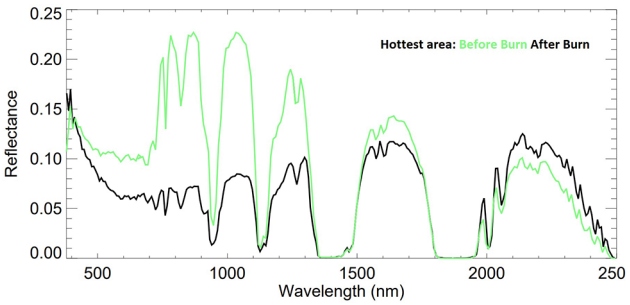

Figure 4. Spectral measurements of Lahaina site over the hottest location, before (Airborne Visible/InfRared Imaging Spectrometer on 26 January 2018) and after the fire (Earth surface Mineral dust source InvesTigation on 18 August 2023)

Disaster Damage Indicators and Recovery with Time Series Analysis

Time series analysis is a powerful technique to study phenomena changes over a period of time, including secular trend, short term variations, cyclic variation, or irregular variations. In this section, we quantify the recovery from the Lahaina fire in Maui and recovery from the hurricane damage in the Gulf of America with a series of satellite observations from VIIRS using the night light intensity and urban greenness as two major indicators of damage caused by natural disasters.

Recovery from Lahaina Fire

Two indices are used to quantify the recovery from fire in this study: the night light intensity from the VIIRS/DNB, and the urban greenness index trend calculated using the NDVI formula with VIIRS I-band observations and *Sentinel-2* bands 4 and 8.

Using the NDVI as a proxy in this study, the urban greenness index can be an important indicator for recovery. Urban green spaces include public or private vegetated areas, such as parks, street trees, grasslands, and residential gardens. They are part of the urban ecosystem and habitats for the residents and serve important functions such as heat reduction, air purification, flood mitigation, and environmental public health benefits for the dwellers' physical, mental, and social well-being (Canada Statistics 2023). During the fire, many trees and gardens were burned, which would reduce the urban greenness. In this study, we first used the *Sentinel-2* NDVI data before and after the fire to analyze the spatial patterns of the urban greenness change within Lahaina city. Then, the NDVI time series from *NOAA-20* VIIRS was used to study the recovery.

Figure 5 (top panels) shows the NDVI change, which reveals the areas of significant changes in urban greenness. Before the fire, the area along the coast was densely vegetated with high greenness along

Front Street. After the fire, a few spots are left unburned. The change in greenness spanned the entire city from latitude of 20.85N to 20.90N, or approximately 5 kilometers from north to south. We identified four major areas (labeled as A, B, C, and D in Figure 5) to represent areas affected by fire. Then, the NDVI time series of the sites are plotted in the bottom panel of Figure 5. It can be seen that areas A and D experienced a major decrease in NDVI due to fire burn, whereas areas of B and C had much smaller changes. The location labeled as T_{max} is where the maximum fire temperature was observed, and its NDVI time series with higher temporal resolution is plotted in Figure 6 as discussed below.

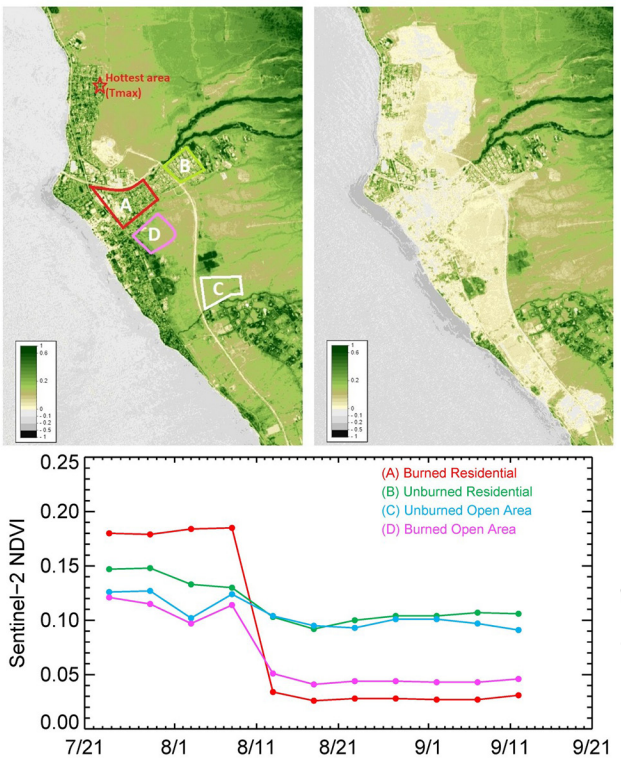

Figure 5. The top panels show the change in urban greenness before (left) and after (right) the fire. The bottom panel shows the Normalized Difference Vegetation Index (NDVI) time series for selected areas from *Sentinel-2*.

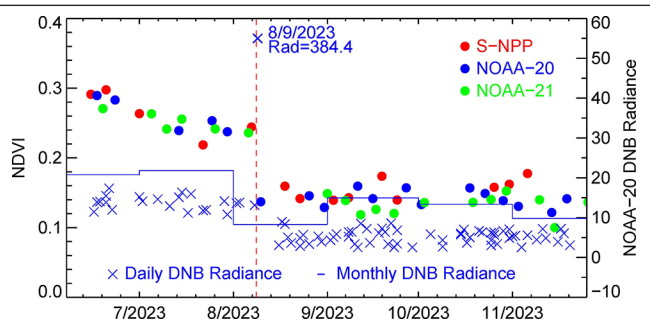

Figure 6. Time series of the urban greenness index (using Normalized Difference Vegetation Index [NDVI]) at the hottest spot location (T_{max}) with colored dots separated by three satellites and the Day/Night Band (DNB) night light intensity at the shopping mall (location: 20.8780, −156.6810) in Lahaina. The solid line represents the monthly composite DNB mean radiance (Earth Observation Group 2023).

The time series in Figure 6 shows that urban greenness exhibits three interesting patterns. First, since June 2023 before the fire, the urban greenness index had been decreasing slowly. The NDVI (far left on the figure) was about 0.28 in June, and it dropped to about 0.26 just before the fire in August, suggesting that the area was suffering from a drought, which may have been one of the contributors to the fire. Second, urban greenness decreased significantly due to the fire event on 8 August. The NDVI value for the hottest spot changed from 0.26 to 0.14, or by 46%. Third, the time series shows the recovery is fairly slow, with a relatively flat line in the NDVI value around 0.14 after the fire. However, we expect it to recover over time due to the resilience of the community.

The use of DNB to study light outages after a disaster has been demonstrated previously (Cao *et al.* 2013; Ghosh 2022). The DNB radiance at the shopping mall site (Outlets of Maui, location: 20.8780, −156.6810) in Lahaina was extracted from the VIIRS observations and a time series was established. As shown in Figure 6, the VIIRS DNB radiance for this location was around 23 nW/cm²-sr in monthly mean value before the fire and was reduced by half after the fire (below 10 nW/cm²-sr). For the day of the fire, the DNB radiance was very high (384.4 nW/cm²-sr) due to the intense flames and was out of the typical range of night light. The trend of the time series suggests that since the fire, the night light has been gradually increasing, which suggests that the infrastructure at that location is recovering slowly. We will continue monitoring the site to see when it will fully recover to previous levels.

Case Studies of Recovery from Hurricanes

Hurricane damage to power lines causes power and light outages and has previously been studied using satellite data. In particular, since the launch of S-NPP VIIRS in 2011, the extremely sensitive VIIRS/DNB images have been used to monitor light outages due to storms and hurricanes and the recovery afterward (Cao *et al.* 2013; Miller *et al.* 2018; NASA 2018). For example, a study shows nighttime light changes in the Washington, DC, metropolitan region from 27 June 27 to 5 July 2012, during which a Direncho swept through the area on 28 June 2012. The night lights gradually recovered 1 week after the event. The light intensity over selected areas in the DC region clearly showed a recovery curve that resembles the RIM model discussed by Lam *et al.* (2016) (Figure 1) despite the differences in the recovery time. In this paper, the DNB data are also used for monitoring the recovery from hurricanes such as Ian, in Tampa, FL, and Ida in New Orleans, respectively.

Figure 7 shows the light outage in the Tampa–Fort Myers, FL, region due to Hurricane Ian. The sudden drop in light intensity (Figure 8) indicates power outages caused by hurricane damage. One caveat is that the DNB lights are affected by clouds, especially during the hurricane attenuating the lights, although the city lights are translucent, which means that some lights could penetrate clouds and reach the satellite sensor. As a result, the light outage and recovery may be affected by clouds, and it is difficult to separate the light outage from clouds, although the VIIRS cloud mask product can help to some extent.

Is there a regional difference in the recovery? We identified 12 sites in the Tampa–Fort Myers area to answer this question. Figure 8b shows that due to Hurricane Ian, all 12 sites suffered light outages. However, the recovery took longer at some locations than others. Specifically, sites #1, #2, #3, and #12 recovered relatively quickly. These sites are found to be on the outskirts of the hurricane's eye. In contrast, power restoration took much longer for sites #4 to #9 (especially the Cape Coral–Fort Myers area in sites #7, #8, and #9), which are much closer to Hurricane Ian's center. This suggests that the recovery is closely tied to the severity of the damage in the RIM model, although resilience is also a factor in the recovery speed.

Figure 9 further shows Moran's I spatial autocorrelation-based analysis (Moran 1950) of DNB radiance data over 4 days in the Cape Coral–Fort Myers and Gasparilla Sound–Charlotte Harbor area. Comparison of Figure 9a and 9b shows that the power outages right after Hurricane Ian in the Cape Coral–Fort Myers and Port Charlotte–Punta Gorda areas are the most severe. Figures 9c and 9d on 3 October 2022 and 8 October 2022 show the spatial extent of the recovery from the power outage in these areas over about 10 days. The average Moran's I index for the entire region shown in Figure 9 changed from 0.57 before the hurricane, to about 0.38 during the power outage and to 0.44 on 8 October 2022. Over the Cape Coral–Fort Myers area, which was along the pathway of the hurricane center, the mean Moran I index

changes from 11.90 on 26 September 2022 to 0.85 on 30 September 2022, right after the pass of the hurricane, to 4.00 on 3 October 2022 during the recovery and to 6.77 on 8 October 2022, which shows the power recovery in this area. Over another area of interest, i.e., Port Charlotte–Punta Gorda area, the mean Moran I index dropped to 0.05 on 30 September 2022, recovered to 0.3 on 3 October 2022, and then recovered further to 0.65 on 8 October 2022.

Another example is Hurricane Ida over New Orleans. In the late morning of 29 August 2021, category 4 Hurricane Ida made landfall near Port Fourchon (NOAA/NWS 2023), Louisiana, on the same day as Hurricane Katrina in 2005. Hurricane Ida quickly intensified over the 3 days before landfall, rapidly going from a tropical depression to a category 4 hurricane. It produced significant wind damage, storm surges, and flash flooding across the Gulf Coast. Its remnants later produced deadly flooding across parts of the Northeastern United States, including New York City, and a regional tornado outbreak along the Interstate 95 corridor from Virginia to New England. Overall, Hurricane Ida caused 87 deaths and an estimated $75 billion in property damage from Louisiana to New England. These statistics are in contrast to Hurricane Katrina in 2005, which caused a total of 1,833 fatalities.

We selected four sites around the New Orleans–Baton Rouge metropolitan area to study the recovery at different locations. Figure 10a shows the four sites on a Sentinel true color map to illustrate where the sample VIIRS/DNB data are taken before, during, and after the hurricane. Figure 10b–e show panels of four selected DNB images before (Figure 10b) and during (Figure 10c–e) the recovery. The Moran I index values of these four selected areas are 0.46, 0.05, 0.09, and 0.41, respectively, which characterizes well the sudden decrease of spatial clustering of night lights and their recoveries over time in this region. These sites were selected to see whether there is any difference in the light intensity change due to outage and time to recover. Figure 10f shows that while all four locations suffered light outages during

Figure 7. *NOAA-20*/Suomi National Polar-Orbiting Partnership Visible Infrared Imaging Radiometer Suite/Day/Night Band (DNB) detection of light outages in the Fort Myers area caused by Hurricane Ian. The left image is from before the hurricane, the middle image is from just after the hurricane, and the right image shows the light values of before minus after. The *Landsat-8* image is used as background. The unit for DNB radiance is nW/(cm²-sr).

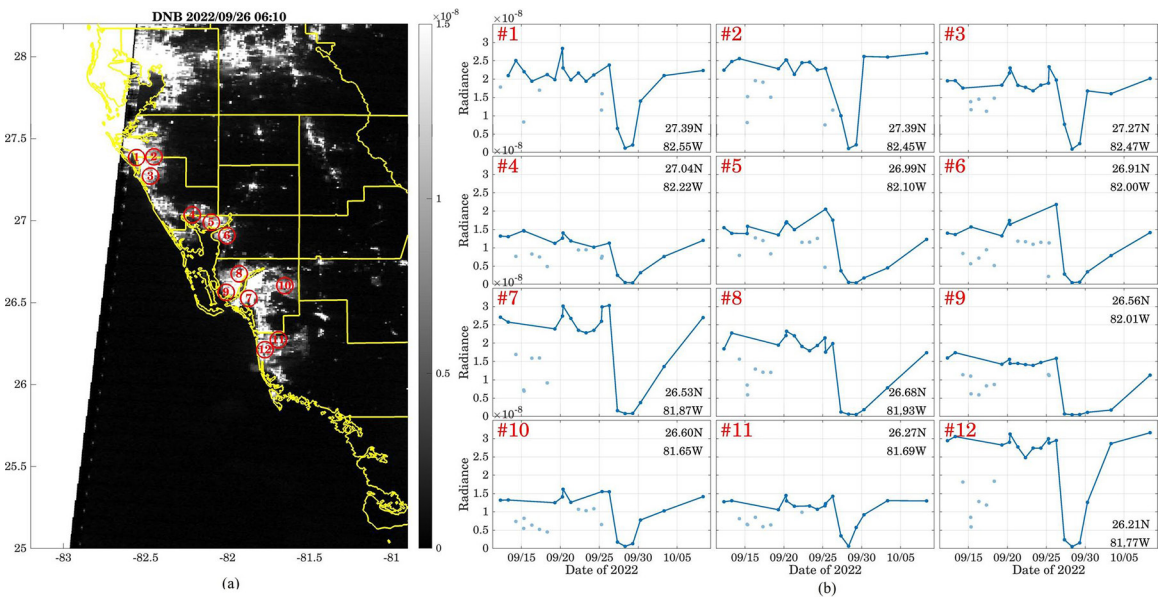

Figure 8. (a) Locations of selected sites for Day/Night Band (DNB) light recovery assessment (radiance > 10−8 W/cm²-sr before Hurricane Ian on 26 September 2022). (b) Recovery of night lights over selected sites after Hurricane Ian. (Unconnected dots indicate cloudy data, which are excluded from the analysis.)

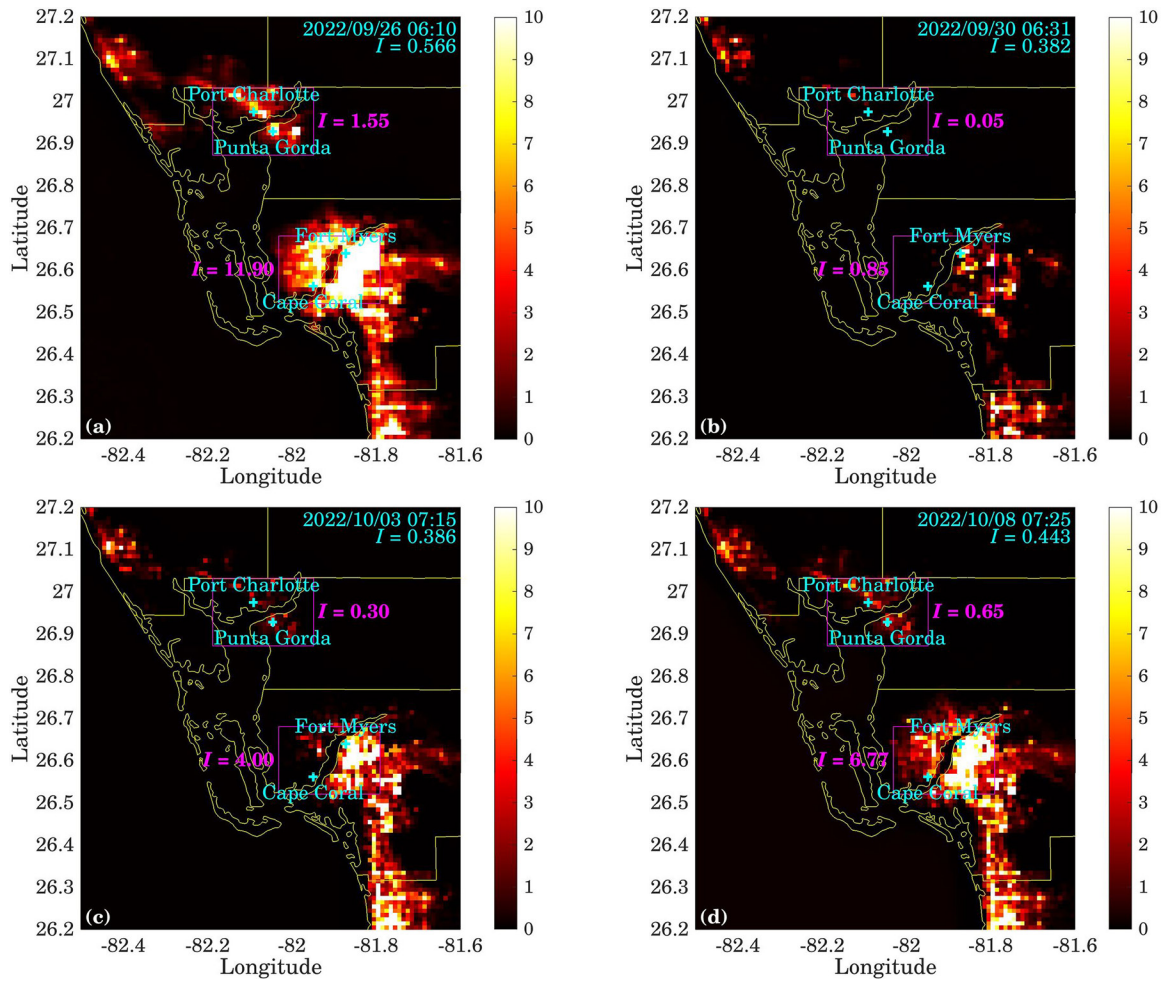

Figure 9. Moran's I spatial correlation analysis of Day/Night Band (DNB) radiance data over 4 days in the Cape Coral–Fort Myers and Gasparilla Sound–Charlotte Harbor areas. The spatial extent of power outage right after Hurricane Ian (b) and during the recovery (c and d) can be assessed by comparison with (a). The overall regional mean Moran's I index is listed at the top right corner of each panel. The pink rectangle and numbers in each panel show the sampling region and corresponding mean Moran's I index in the regions around Cape Coral–Fort Myers and Port Charlotte–Punta Gorda areas.

the hurricane, the severity is different. For example, site 4 (the Baton Rouge region) suffered relatively smaller outages and recovered quickly. Site 1 (west New Orleans) recovered relatively slowly in comparison with site 2 (New Orleans), which can also be seen by comparing the light maps near New Orleans in Figure 10b-e. This indicates that the time series analysis reveals the different recovery speeds between nearby sites such as sites 1 and 2. Site 3 (Slidell, LA) appears to have recovered fairly quickly, possibly due to a couple of factors. First, this is a growing community close to the NASA Stennis Space Center; therefore, the infrastructure is relatively newer. Second, this community took a major hit during Hurricane Katrina, and the infrastructure may be upgraded and better prepared for future hurricanes (adaptability). The mean night light radiances before (12 to 28 August) over the four selected sites are 53.0 ± 6.5, 55.2 ± 10.4, 24.4 ± 4.4, and 39.4 ± 4.3 W/cm²-sr, respectively, and the mean radiances after the hurricane (5 to 12 September) are 27.9 ± 12.8, 49.1 ± 11.9, 23.4 ± 1.5, and 42.9 ± 6.1 W/cm²-sr, respectively. This indicates that site 2 to 4 recovered from the power outage by 5 September, whereas site 1 was still under recovery until 10 September. This result suggests that the short-term recovery speed from storm damage is closely tied to the resilience of the community, which is a crucial factor in the RIM model.

Figure 10f also shows that, after recovering from Hurricane Ida, the night light took another deep dive around 15 September. Further investigation shows that this is likely due to the remnants of Hurricane Nicholas. From 15 to 16 September, 2021, Tropical Depression Nicholas continued slowly eastward across southern Louisiana, making an anticyclonic loop on 16 September. Nicholas was designated post-tropical due to the lack of convection early on 17 September while it headed northward across central Louisiana, dissipating later that evening across northern Louisiana. However, the DNB data taken were too cloudy, and the light outage cannot be accurately estimated (shown as crosses in the figure).

Discussion on Community Vulnerability and Adaptability to Natural Disasters and Our Contributions to the RIM Model

Vulnerability, a complex interplay of exposure, sensitivity, and adaptive capacity, is integral to understanding a population's response to natural hazards (Cutter *et al.* 2003). Lam *et al.* (2016) emphasize that vulnerability encapsulates elements of resilience. This discussion assesses the vulnerability of Lahaina in Maui to fires and the Gulf Coast of America to hurricanes.

Maui's diverse climatic conditions, influenced by various physical factors, result in distinct climate regions. Figure 11 shows that the mean annual precipitation at Lahaina is less than 10 inches, located at the base of the mountains on the leeward side, and has a hot, semi-arid climate type despite its coastal location with low elevation. It also faces unique challenges because the strong downslope "lehua" winds can reach speeds of 80 to 100 mph, which makes Lahaina susceptible to rapid fire spread. The 2023 Lahaina fire underscored the previously underestimated fire hazard, prompting increased awareness and preparedness among the community.

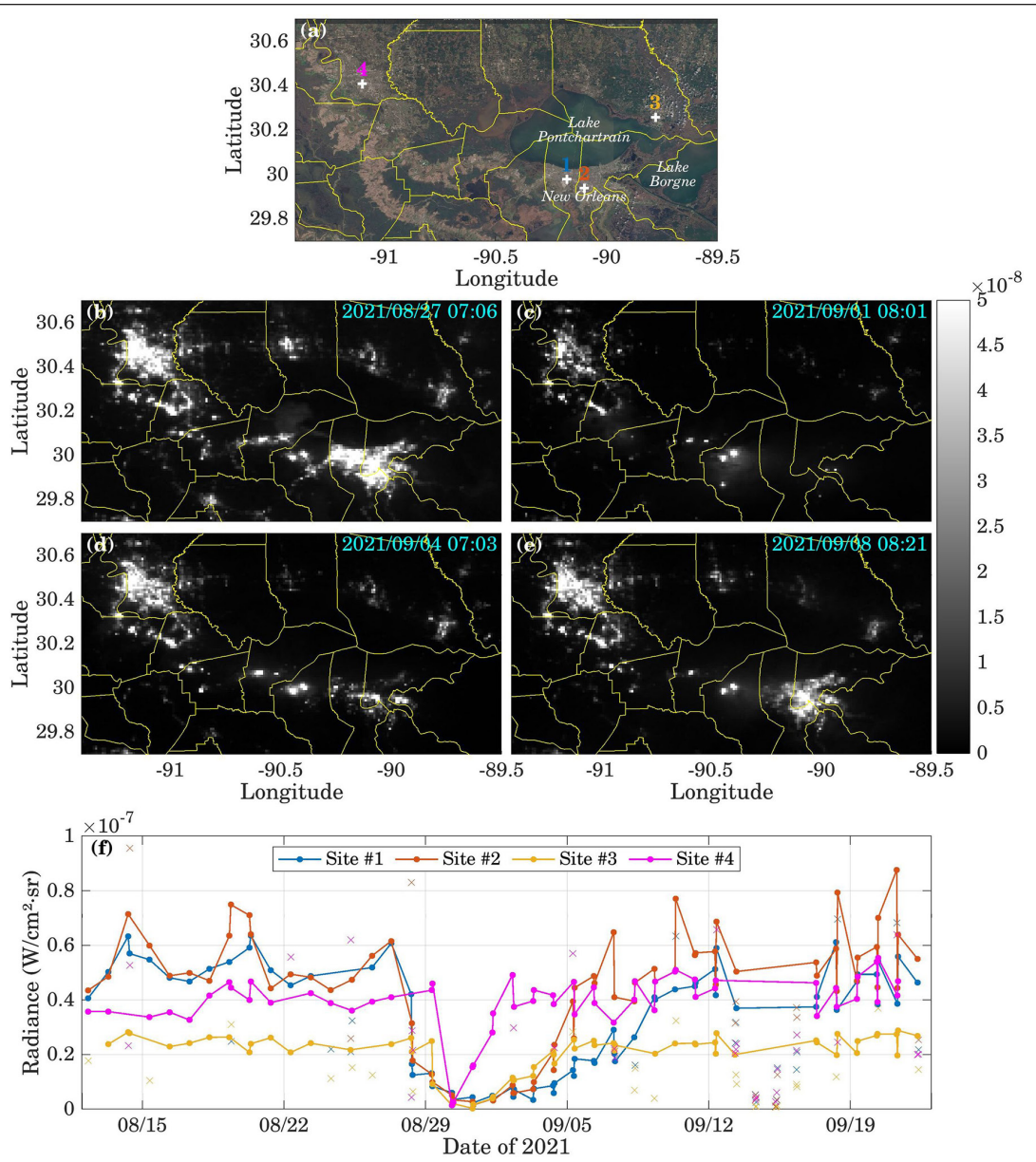

Figure 10. Night light intensity time series measured by *NOAA-20* Visible Infrared Imaging Radiometer Suite/Day/Night Band (DNB). (a) Four selected sites around New Orleans-Baton Rouge marked on Sentinel true color map with yellow county lines. (b–e) Four selected DNB images before (b) and during (c–e) the recovery. (f) DNB radiance time series for four sites over the recovery with cloudy data identified and lunar radiance subtracted (unconnected × data points indicate cloudy data, which are excluded from the analysis).

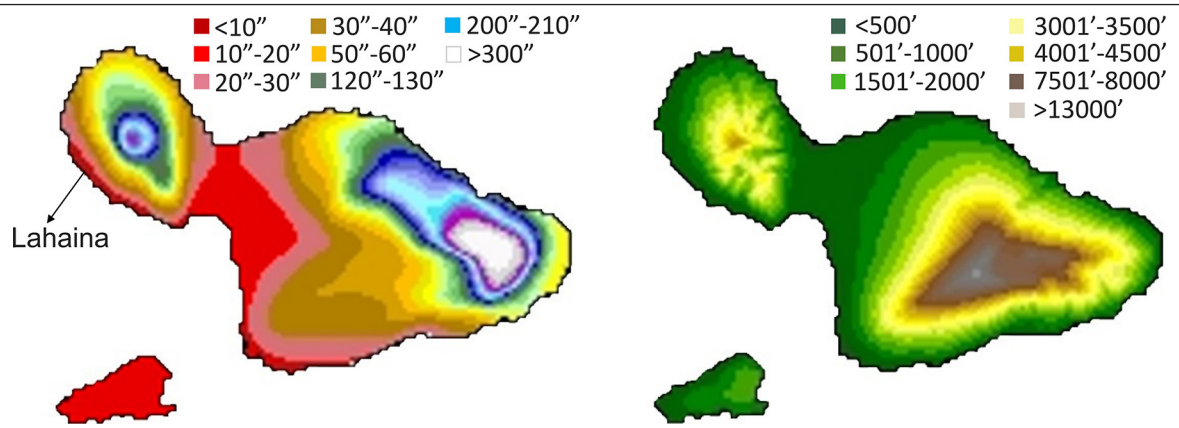

Figure 11. Maui mean annual precipitation (left) and digital elevation model (right) (PRISM Climate Group 2012).

In contrast, the Gulf Coast of America experiences a hot and humid tropical/subtropical climate, making it prone to hurricanes. The gulf's geographical location contributes to the high frequency of hurricanes. Warm waters, convergence of air masses, favorable atmospheric conditions, and seasonal patterns collectively create an environment conducive to hurricane formation. Florida and New Orleans, both susceptible to hurricanes, exhibit vulnerabilities due to extensive coastlines and low-lying topography.

The communities in Lahaina and the Gulf of America must acknowledge the hazards and risks associated with their geolocation and physical environment. The probability of damages from natural disasters is heightened, necessitating thorough preparedness, especially in the context of escalating climate change and variability.

This discussion underscores the critical importance of understanding vulnerability dynamics and fostering resilience in communities facing diverse natural hazards. It emphasizes the need for continuous adaptation strategies and heightened awareness to mitigate the effects of these events on both life and property.

As discussed earlier, the RIM model provided an excellent framework for connecting the dots among various elements associated with natural disasters from exposure and damage to recovery and the resilience developed in the community in the iterative process of adaptation and mitigation to reduce vulnerability. Lam *et al.* (2016) demonstrated the model efficacy by using population growth over decades as an indicator of recovery. Our study further augments the RIM model by incorporating satellite observation and related indices, such as urban greenness, night light intensity, Moran's I index, and wildfire dynamics. These indicators complement the RIM model with more quantitative measures of damage, recovery, and resilience and can be used as indicators with a much shorter time frame of days or weeks instead of decades. This also demonstrates the value of using remote sensing observations to facilitate more broad use of the RIM model for a variety of applications.

Conclusions

In this study, we have demonstrated the efficacy of using satellite observations to assess and quantify the effect and recovery of selected communities in the aftermath of natural disasters, complementing the RIM. Focusing on the Maui fire in 2023 and hurricanes along the Gulf of America coast, our approach involves time series analysis of urban greenness and night light intensity to gauge recovery.

For the Maui fire, we pinpointed the timeframe of peak brightness temperature using GOES ABI thermal infrared images, identified the location of the hottest spot (T_{max}) in north Lahaina, and conducted time series analysis of urban greenness and night light changes. In the case of Gulf Coast hurricanes, we analyzed night light changes in the aftermath of Hurricane Ian over Tampa–Fort Myers, FL, and Ida over New Orleans.

Our findings reveal that satellite-derived indices, such as urban greenness, night light intensity, and Moran's I index, serve as valuable quantitative measures for monitoring both short-term and long-term community recovery and can be included in the framework of the RIM model for assessing damage, recovery, and resilience. This methodology significantly enhances the RIM model, which traditionally relies on socioeconomic parameters spanning decades. We believe that satellite assets contribute substantial value to the comprehensive assessment of recovery within the framework of the RIM model.

Moreover, our examination of the vulnerabilities of Maui to fires and the Gulf of America to hurricanes using the RIM model underscores the resilience of these communities. We anticipate that the lessons learned from these disasters will contribute to enhanced preparedness, making these communities more resilient in future catastrophic events.

Acknowledgments

This paper contributes to the *PE&RS* special issue for Professor Nina Lam in celebration of her 45+ years of outstanding mentorship and scholarly achievements. Her guidance, wisdom, and dedication have been a source of inspiration to all of us, her students. We thank the anonymous reviewers for the thorough and rigorous reviews with constructive comments and suggestions, which led to significant improvements in our manuscript. We also thank Tung-Chang Liu for graphic work assistance. This study is partially supported by NOAA/NESDIS/STAR and NOAA grants NA19NES4320002 and NA24NESX432C0001 (CISESS/ESSIC, University of Maryland). The manuscript contents are solely the opinions of the authors and do not constitute a statement of policy, decision, or position on behalf of NOAA or the U.S. government.

References

Adger, W., K. Brown and D. Conway. 2010. Progress in global environmental change. *Global Environmental Change* 20:547–549.

Bathiany, S., R. Bastiaansen, A. Bastos, L. Blaschke, J. Lever, S. Loriani, W. De Keersmaecker, W. Dorigo, M. Milenković, C. Senf, T. Smith, J. Verbesselt and N. Boers. 2024. Ecosystem resilience monitoring and early warning using earth observation data: Challenges and outlook. *Surveys in Geophysics*. https://doi.org/10.1007/s10712-024-09833-z.

Canada Statistics. 2023. Census of environment: Urban greenness. <https://www150.statcan.gc.ca/n1/daily-quotidien/231115/dq231115c-eng.htm> (last date accessed: 17 December 2024).

Cao, C., F. J. De Luccia, X. Xiong, R. Wolfe and F. Weng. 2014. Early on-orbit performance of the Visible Infrared Imaging Radiometer Suite onboard the Suomi National Polar-Orbiting Partnership (S-NPP) satellite. *IEEE Transactions on Geoscience and Remote Sensing* 52(2):1142–1156. https://doi.org/10.1109/TGRS.2013.2247768.

Cao, C., X. Shao and S. Uprety. 2013. Detecting Light Outages after Severe Storms Using the S-NPP/VIIRS Day/Night Band Radiances. *IEEE Geoscience and Remote Sensing Letters* 10(6):1582–1586. https://doi.org/10.1109/LGRS.2013.2262258.

Cao, C., B. Zhang, X. Shao, W. Wang, S. Uprety, T. Choi, S. Blonski, Y. Gu, Y. Bai, L. Lin and S. Kalluri. 2021. Mission-long recalibrated science quality Suomi NPP VIIRS radiometric dataset using advanced algorithms for time series studies. *Remote Sensing* 13(6):1075. https://doi.org/10.3390/rs13061075.

Csiszar, I., W. Schroeder, L. Giglio, E. Ellicott, K. P. Vadrevu, C. O. Justice and B. Wind. 2014. Active fires from the Suomi NPP Visible Infrared Imaging Radiometer Suite: Product status and first evaluation results. *Journal of Geophysical Research: Atmospheres*. 119(2):803–816.

Cutter, S. L., B. J. Boruff and W. L. Shirley. 2003. Social vulnerability to environmental hazards. *Social Science Quarterly* 84(2):242–261.

Earth Observation Group. 2023. See the world at night. <https://eogdata.mines.edu/products/vnl/> (last date accessed: 17 December 2024).

Elvidge, C. D., M. Zhizhin, F.-C. Hsu and K. E. Baugh. 2013. VIIRS Nightfire: Satellite pyrometry at night. *Remote Sensing* 5(9):4423–4449. https://doi.org/10.3390/rs5094423.

eoPortal. 2023. Satellite missions. <https://www.eoportal.org/satellite-missions> (last date accessed: 17 December 2024).

Ghosh, T. 2022. Power outage in Florida caused by Hurricane Ian. <https://payneinstitute.mines.edu/power-outage-in-florida-caused-by-hurricane-ian> (last date accessed: 17 December 2024).

Green, R., M. L. Eastwood, C. M. Sarture, T. G. Chrien, M. Aronsson, B. J. Chippendale, J. A. Faust, B. E. Pavri, C. J. Chovit, M. Solis, M. R. Olah and O. Williams. 1998. Imaging spectroscopy and the airborne visible/infrared imaging spectrometer (AVIRIS). *Remote Sensing of Environment* 65(3):227–248.

Green, R. 2022. EMIT mission data products. <https://lpdaac.usgs.gov> (last date accessed: 17 December 2024).

Green, R. O., N. Mahowald, C. Ung, D. R. Thompson, L. Bator, M. Bennet, M. Bernas, N. Blackway, C. Bradley, J. Cha, P. Clark, R. Clark, D. Cloud, E. Diaz, E. B. Dor, R. Duren, M. Eastwood, B. L. Ehlmann, L. Fuentes, P. Ginoux, J. Gross, Y. He, O. Kalashnikova, W. Kert, D. Keymeulen, M. Klimesh, D. Ku, H. Kwong-Fu, E. Liggett, L. Li, S. Lundeen, M. D. Makowski, A. Mazer, R. Miller, P. Mouroulis, B. Oaida, G. S. Okin, A. Ortega, A. Oyake, H. Nguyen, T. Pace, T. H. Painter, J. Pempejian, C. P. Garcia-Pando, T. Pham, B. Phillips, R. Pollock, R. Purcell, V. Realmuto, J. Schoolcraft, A. Sen, S. Shin, L. Shaw, M. Soriano, G. Swayze, E. Thingvold, A. Vaid and J. Zan. 2020. The earth surface mineral dust source investigation: An earth science imaging spectroscopy mission. *Proceedings of the 2020 IEEE Aerospace Conference*, 7–14 March 2020, Big Sky, Montana, pp. 1–15.

Intergovernmental Panel on Climate Change. 2007. Climate change 2007: Synthesis report. In *Contribution of Working Groups I, II and III to the Fourth Assessment Rep. of the Intergovernmental Panel on Climate Change,* edited by R. K. Pachauri and A. Reisinger, Vol. 104, Geneva, Switzerland: Intergovernmental Panel on Climate Change.

Kerber, S. and D. Alkonis. 2024. *Lahaina Fire Comprehensive Timeline Report*. Columbia, MD: U.S. Fire Administration/Fire Safety Research Institute. https://doi.org/10.54206/102376/VQKQ5427.

Lam, N. S. N., Y. Qiang, K. Li, H. Cai, L. Zou and M. Volodymyr. 2018. Extending resilience assessment to dynamic system modeling: Perspectives on human dynamics and climate change research. *Journal of Coastal Research* 85(sp1):1401–1405.

Lam, N. S. N., M. Reams, K. Li, C. Li and L. P. Mata. 2016. Measuring community resilience to coastal hazards along the northern Gulf of Mexico. *Natural Hazards Review* 17(1):04015013. https://doi.org/10.1061/(ASCE)NH.1527-6996.0000193.

Miller, S., W. Straka III, J. Yue, C. Seaman, S. Xu, C. Elvidge, L. Hoffmann and I. Azeem. 2018. The dark side of Hurricane Matthew: Unique perspectives from the VIIRS day/night band. *Bulletin of the American Meteorological Society* 99(12):2561–2574. https://doi.org/10.1175/BAMS-D-17-0097.1.

Moran, P.A.P. 1950. Notes on continuous stochastic phenomena. *Biometrika* 37(1):17–23. https://doi.org/10.2307/2332142.

NASA. 2018. Night lights show slow recovery from Maria. <https://earthobservatory.nasa.gov/images/144371/night-lights-show-slow-recovery-from-maria> (last date accessed: 17 December 2024).

National Research Council. 2012. *Disaster resilience: A national imperative.* Washington, DC: National Academies Press. https://doi.org/10.17226/13457.

NOAA. 2023. Hurricane costs. NOAA Office for Coastal Management. <https://coast.noaa.gov/states/fast-facts/hurricane-costs.html#:~:text=Of%20all%20recorded%20weather%20disasters,the%20most%20deaths%20and%20destruction> (last date accessed: 17 December 2024).

NOAA/NWS. 2023. Service assessment: August–September 2021 Hurricane Ida, <https://www.weather.gov/media/publications/assessments/Hurricane_Ida_Service_Assessment.pdf> (last date accessed: 17 December 2024).

Peduzzi, P., H. Dao, C, Herold and F. Mouton. 2009. Assessing global exposure and vulnerability towards natural hazards: The disaster risk index. *Natural Hazards and Earth System Sciences* 9:1149–1159.

Piper, I., J. Lee, E. Izadi and B. Sacks. 2023. Maui's neglected grasslands caused Lahaina fire to grow with deadly speed, *Washington Post*. <https://www.washingtonpost.com/investigations/interactive/2023/lahaina-wildfires-invasive-grass-destruction/> (last date accessed: 17 December 2024 year).

PRISM Climate Group. 2012. PRISM Climate Data. (Map created 25 January 2012.) Oregon State University, Corvallis, Oregon. <https://prism.oregonstate.edu> (last date accessed: 17 December 2024).

Schulz, B. and T. Collins. 2023. Devastating losses: Economic toll from Maui fires at least $4 billion, Moody's projects. *USA Today*. <https://www.usatoday.com/story/money/2023/08/23/maui-fires-economic-cost/70659021007/> (last date accessed: 17 December 2024).

Statista. 2023. Number of orbital space launches worldwide from 1957 to 2022. Statista Research Department. <https://www.statista.com/statistics/1343344/orbital-space-launches-global/#:~:text=After%20decelerating%20in%20the%2090s,the%20Space%20Race%20in%201957> (last date accessed: 17 December 2024).

Thompson, D. R., R. O. Green, C. Bradley, P. G. Brodrick, N. Mahowald, E. B. Dor, M. Bennett, M. Bernas, N. Carmon, K. D. Chadwick, R. N. Clark, R. W. Coleman, E. Cox, E. Diaz, M. L. Eastwood, R. Eckert, B. L. Ehlmann, P. Ginoux, M. G. Ageitos, K. Grant, L. Guanter, D. H. Pearlshtien, M. Helmlinger, H. Herzog, T. Hoefen, Y. Huang, A. Keebler, O. Kalashnikova, D. Keymeulen, R. Kokaly, M. Klose, L. Li, S. R. Lundeen, J. Meyer, E. Middleton, R. L. Miller, P. Mouroulis, B. Oaida, V. Obiso, F. Ochoa, W. Olson-Duvall, G. S. Okin, T. H. Painter, C. Pérez García-Pando, R. Pollock, V. Realmuto, L. Shaw, P. Sullivan, G. Swayze, E. Thingvold, A. K. Thorpe, S. Vannan, C. Villarreal, C. Ung, D. W. Wilson and S. Zandbergen. 2024. On-orbit calibration and performance of the EMIT imaging spectrometer. *Remote Sensing of Environment* 303:113986.

Tierney, K. and A. Oliver-Smith. 2012. Social dimensions of disaster recovery. *International Journal of Mass Emergencies and Disasters* 30:123–146.

Vogel, C. 2006. Foreword: Resilience, vulnerability and adaptation: A cross-cutting theme of the International Human Dimensions Programme on Global Environmental Change. *Global Environmental Change* 16:235–236.

Walker, B., L. Gunderson, A. Kinzig, C. Folke, S. Carpenter and L. Schultz. 2006a. A handful of heuristics and some propositions for understanding resilience in social–ecological systems. *Ecology and Society*, 11(1):13.

Walker, B. H., J. M. Anderies, A. P. Kinzig and P. Ryan. 2006b. Exploring resilience in social–ecological systems through comparative studies and theory development: Introduction to the special issue. *Ecology and Society* 11(1):12.

Wang, W., C. Cao, S. Blonski, Y. Gu, B. Zhang and S. Uprety. 2022. An improved method for VIIRS radiance limit verification and saturation rollover flagging. *IEEE Transactions on Geoscience and Remote Sensing* 60:1–11.